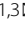



ARTICLE

Open Access

Lanthanide-based metal halides prepared at room temperature by recrystallization method for X-ray imaging

Huwei Li^{1,2}, Kai Li¹, Zheyu Li^{1,3}, Xinyu Fu^{1,3}, Qingxing Yang^{1,3}, Nan Wang^{1,3}, Xinyu Wang¹, Jing Feng^{1,3} , Shuyan Song^{1,3}  and Hongjie Zhang^{1,2,3,4} 

Abstract

Lanthanide (Ln)-based metal halides with excellent luminescence properties, large Stokes shifts, and low toxicity have aroused wide attention as scintillators for X-ray imaging. However, the lack of fast and mild synthesis methods of Ln-based metal halides, as one of the technical challenges, limits their applications. Here, benefiting from the innovative selection of methanol and ethanol as the solvent and anti-solvent, respectively, a series of Cs_3LnCl_6 (Ln = Ce, Pr, Nd, Sm, Eu, Gd, Tb, Dy, Ho, Er, Tm, Yb, Lu) microcrystals (MCs) were prepared via the recrystallization method at room temperature for the first time. This recrystallization method could also realize large-scale production at one time and recyclable recrystallization of single-element MCs and the preparation of high-entropy five-element $\text{Cs}_3(\text{TbDy-HoErTm})\text{Cl}_6$ crystals. Among these Cs_3LnCl_6 MCs, Cs_3TbCl_6 MCs with $4f \rightarrow 5d$ absorption transition possess the highest photoluminescence quantum yield of 90.8%. Besides, under X-ray irradiation, Cs_3TbCl_6 MCs show a high light yield of $\sim 51,800$ photons MeV^{-1} and the as-fabricated thin films possess promising X-ray imaging ability and excellent spatial resolutions (12 lp mm^{-1}). This work provides a new method for ultrafast preparing Ln-based metal halides under mild synthetic conditions and highlights their excellent potential as scintillators for X-ray imaging.

Introduction

X-ray scintillators can convert X-ray photons to visible photons with lower energy and have been widely employed in the fields of industrial flaw detection, medical diagnosis, safety inspection, petroleum logging, environmental monitoring, etc. Recently, lead-based metal halides with large X-ray absorption coefficients, excellent photoelectric properties and solution processability have displayed remarkable scintillation performance and great promise for X-ray detection and imaging^{1–7}. However, the toxicity of Pb^{2+} and self-absorption caused by small Stokes shifts inhibit their large-scale applications as scintillators. To overcome these issues, replacing Pb^{2+}

with other elements to obtain lead-free metal halides with low toxicity and large Stokes shifts has captured great interest^{8–12}.

Trivalent lanthanide (Ln^{3+}) ions with low toxicity, large Stokes shifts, and distinct energy level transitions usually exhibit abundant and unique emissions with sharp lines in the range from ultraviolet (UV) to near-infrared (NIR) region^{13–15}. Besides, quantum yield improvement, quantum cutting effect, defects passivation, multimode luminescence, etc., caused by the introduction of Ln^{3+} ions dopants, can bring lead-free metal halides excellent potentials in the applications of X-ray imaging, solid-state lighting, night vision, information storage, optical thermometry, etc.^{16–23}. To date, there are many reports on Ln-doped metal halides²⁴, but a few on Ln-based metal halides due to the difficulty in synthesis, which limits the development of Ln-based metal halides as scintillators in the field of X-ray imaging. According to the previous reports, it is difficult to prepare Ln-based metal halides with high crystallinity by the traditional solvothermal

Correspondence: Jing Feng (fengj@ciac.ac.cn) or Shuyan Song (songsy@ciac.ac.cn) or Hongjie Zhang (hongjie@ciac.ac.cn)

¹State Key Laboratory of Rare Earth Resource Utilization, Changchun Institute of Applied Chemistry, Chinese Academy of Sciences, Changchun 130022, China

²State Key Laboratory of Inorganic Synthesis and Preparative Chemistry, College of Chemistry, Jilin University, Changchun 130012, China

Full list of author information is available at the end of the article

© The Author(s) 2025



Open Access This article is licensed under a Creative Commons Attribution 4.0 International License, which permits use, sharing, adaptation, distribution and reproduction in any medium or format, as long as you give appropriate credit to the original author(s) and the source, provide a link to the Creative Commons licence, and indicate if changes were made. The images or other third party material in this article are included in the article's Creative Commons licence, unless indicated otherwise in a credit line to the material. If material is not included in the article's Creative Commons licence and your intended use is not permitted by statutory regulation or exceeds the permitted use, you will need to obtain permission directly from the copyright holder. To view a copy of this licence, visit <http://creativecommons.org/licenses/by/4.0/>.

method because Ln elements have strong oxygen affinity and hydrophilicity, and the solubility of Ln halides is quite different from other metal halides in mixed solutions²⁵. Although there have been some reports of Ln-based metal halides synthesized by high-temperature solid-state synthesis or hot-injection method, such high-temperature conditions extremely limit their development^{26–29}. Hence, it is necessary to develop a simple, fast, and mild synthesis method to prepare Ln-based metal halides and further explore their potential as scintillators in the field of X-ray imaging.

Herein, a series of Cs_3LnCl_6 (Ln = Ce, Pr, Nd, Sm, Eu, Gd, Tb, Dy, Ho, Er, Tm, Yb, Lu) metal halide microcrystals (MCs) were synthesized via a recrystallization method at room temperature. Based on this method, the feasibility of large-scale production at one time and recyclable recrystallization of single-element MCs, and the preparation of related high-entropy Ln-based metal halide crystals were investigated. Density functional theory (DFT) calculations were adopted to explore the $4f \rightarrow 5d$ transitions or $\text{Cl} \rightarrow \text{Ln}$ charge transfer transitions in parts of Cs_3LnCl_6 MCs, which could overcome $4f \rightarrow 4f$ parity-forbidden transitions and bring them better absorption ability in the near UV region and great PL performance. Subsequently, Cs_3TbCl_6 , with the highest photoluminescence quantum yield (PLQY) of 90.8% among these Cs_3LnCl_6 , was selected to investigate the potential in the application of X-ray imaging. Under X-ray irradiation, Cs_3TbCl_6 MCs powder with excellent X-ray scintillation performance was combined with polydimethylsiloxane (PDMS) to fabricate related thin films, which displayed great X-ray imaging ability.

Results

Considering the radioactivity of Pm^{3+} , Ln^{3+} ions involved in this work do not include Pm^{3+} . All the samples were prepared through a simple synthetic route at room temperature. As illustrated in Fig. 1a, CsCl and $\text{LnCl}_3 \cdot x\text{H}_2\text{O}$ were dissolved in methanol (MeOH) under ultrasound, and then Cs_3LnCl_6 (Ln = Ce, Pr, Nd, Sm, Eu, Gd, Tb, Dy, Ho, Er, Tm, Yb, Lu) metal halides MCs can be obtained quickly within 2 min by introducing moderate ethanol (EtOH) into the mixed MeOH solution to precipitate them as powder. To prepare Cs_3LaCl_6 , it requires the addition of cyclohexane as an anti-solvent after adding EtOH. However, the obtained metal halide is $\text{Cs}_3\text{LaCl}_6 \cdot 3\text{H}_2\text{O}$ rather than Cs_3LaCl_6 . The structural and morphological characterizations of as-prepared $\text{Cs}_3\text{LaCl}_6 \cdot 3\text{H}_2\text{O}$ are shown in Supplementary Fig. S1. Therefore, in subsequent discussions, we will focus on the remaining thirteen Cs_3LnCl_6 MCs (Ln = Ce, Pr, Nd, Sm, Eu, Gd, Tb, Dy, Ho, Er, Tm, Yb, Lu).

The X-ray diffraction (XRD) patterns of the prepared Cs_3LnCl_6 MCs are displayed in Fig. 1b, Supplementary Fig. S2–9 and S10–14. Cs_3LnCl_6 MCs exhibit similar

diffraction patterns, suggesting these MCs share the same crystal structure and space group. Specifically, the diffraction patterns of Cs_3CeCl_6 , Cs_3PrCl_6 , Cs_3NdCl_6 , Cs_3SmCl_6 , Cs_3EuCl_6 , Cs_3GdCl_6 , Cs_3TbCl_6 , and Cs_3ErCl_6 match well with the standard patterns (PDF#04-007-9649, 04-007-9650, 04-007-9651, 04-007-9652, 04-007-9653, 04-007-9654, 04-006-9440, 04-010-7422), conforming to monoclinic crystal structure ($C2/c$ space group) without any secondary phases (Supplementary Figs. S2–9). Nevertheless, the XRD patterns of Cs_3DyCl_6 , Cs_3HoCl_6 , Cs_3TmCl_6 , Cs_3YbCl_6 , and Cs_3LuCl_6 are not filed in the PDF or ICSD database. Hence, the Rietveld refinements of their diffraction patterns were performed. As shown in Supplementary Fig. S10–14 and Table S1, the Rietveld refinement X-ray diffraction plots and structural parameters of Cs_3DyCl_6 , Cs_3HoCl_6 , Cs_3TmCl_6 , Cs_3YbCl_6 , and Cs_3LuCl_6 were provided, and the results demonstrate their monoclinic crystal structure ($C2/c$ space group) without any secondary phases. Therefore, the crystal structure of all Cs_3LnCl_6 MCs adopts a monoclinic $C2/c$ space group (#15) (Fig. 1a), consisting of a 0D framework of spatially independent octahedra $[\text{LnCl}_6]^{3-}$, which are completely separated by surrounding Cs^+ ions²⁷. Meanwhile, from Cs_3CeCl_6 to Cs_3LuCl_6 , the XRD peak ($\bar{1}13$) slightly shifts to a larger angle. This progressive shrinking of the lattice can be attributed to the gradual reduction of ionic radius from Ce^{3+} to Lu^{3+} . Compared with the XRD patterns of other Cs_3LnCl_6 , the relative intensity between parts of the XRD peaks changes in Cs_3CeCl_6 for the crystals could grow selectively along with different crystal planes. As displayed in the scanning electron microscopy (SEM) images (Fig. 1c), from Cs_3CeCl_6 to Cs_3LuCl_6 , their morphologies transform from thin plate shape to flower shape, which implies the different crystal growth processes, possibly caused by the increasing rate of crystallization. Subsequently, the crystallization rates of these Cs_3LnCl_6 MCs are reflected by the productivities after adding EtOH for 60 seconds. As presented in Supplementary Fig. S15, the crystallization rates become faster and faster from Cs_3CeCl_6 to Cs_3EuCl_6 , and then almost identical from Cs_3EuCl_6 to Cs_3LuCl_6 , which matches well with morphological change in SEM images³⁰.

In addition, this recrystallization method could also realize large-scale production at one time and excellent recyclability of single-element Cs_3LnCl_6 MCs and the preparation of high-entropy five-element Ln-based metal halide crystals. As shown in Fig. 2a, large quantities of Cs_3TbCl_6 MCs (~11.0 g) can be easily obtained at one time by enlarging metal salts in equal proportions by a factor of 100 and dissolving them in MeOH, followed by adding anti-solvent EtOH. Subsequently, the recyclability of as-prepared MCs was explored to avoid the waste of resources after completing a specific application mission. An appropriate amount of MeOH was employed to recover as-prepared Cs_3TbCl_6 MCs. Then, Cs_3TbCl_6 MCs

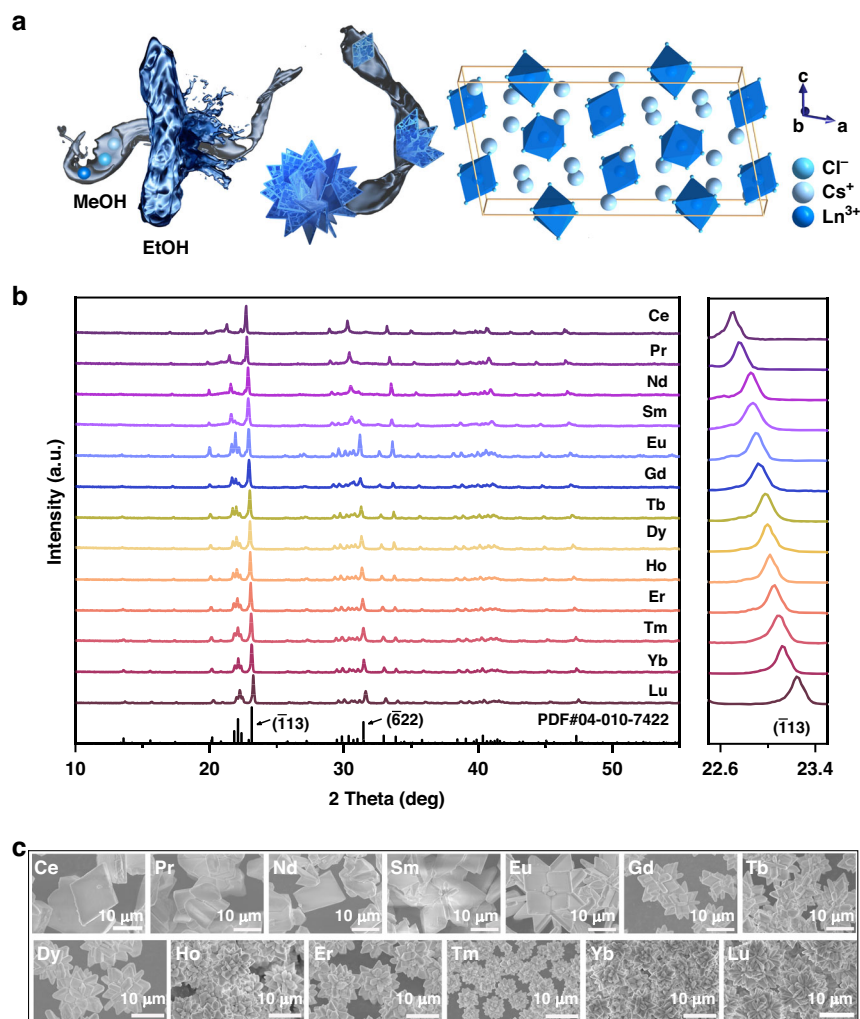
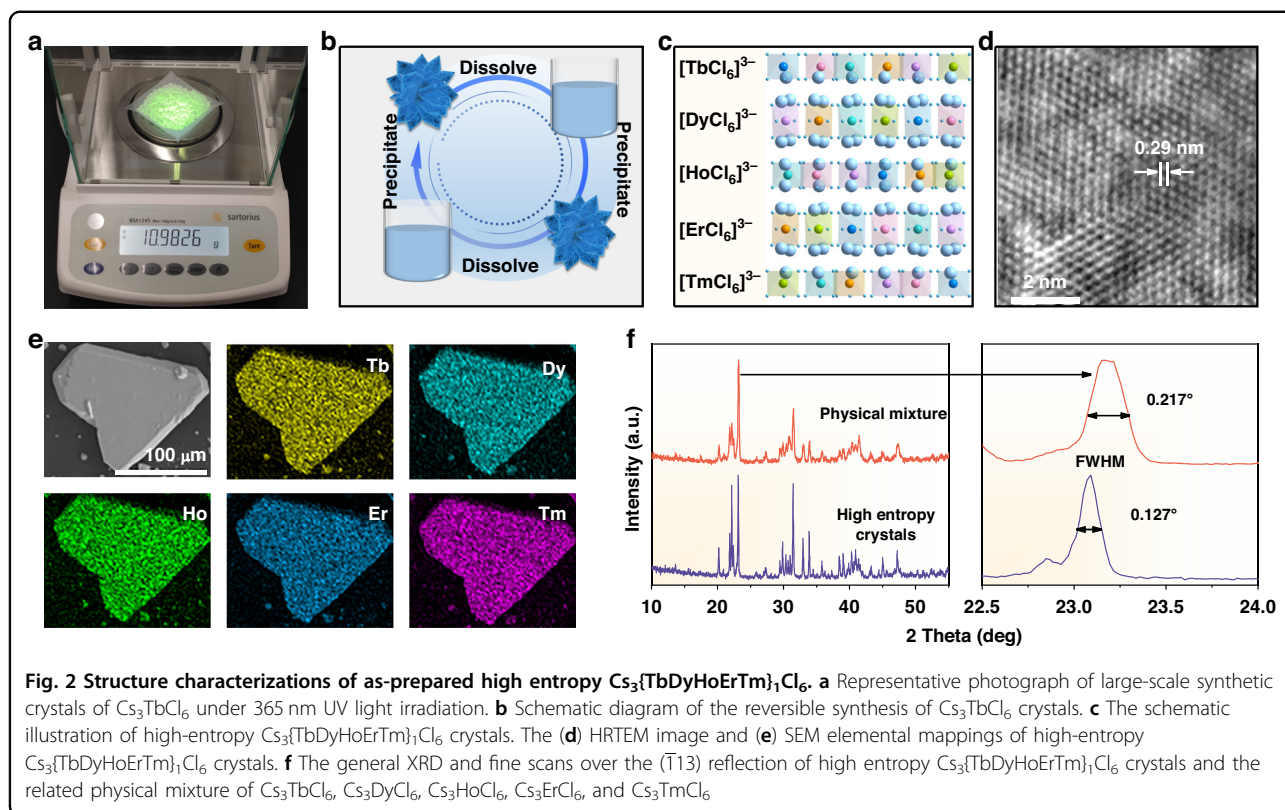


Fig. 1 Structure characterizations of as-prepared Cs_3LnCl_6 . **a** The schematic illustration of the synthesis procedure and crystal unit cell structure of Cs_3LnCl_6 MCs. **b** The powder XRD patterns and **(c)** SEM images of Cs_3LnCl_6 MCs

could be precipitated again with sufficient EtOH as an anti-solvent. As shown in Fig. 2b and Supplementary Fig. S16, Cs_3TbCl_6 MCs could be utilized and recycled repeatedly. In addition, based on this recrystallization method, high-entropy five-element Ln-based metal halide crystals could be prepared successfully. High-entropy materials, as excellent functional materials, have attracted increasing attention, however, high temperature ($\sim 1000^\circ\text{C}$) is generally necessary in synthetic procedures that limits their development^{31,32}. Here, instead of being indirectly added, EtOH as anti-solvent was diffused slowly into the mixed MeOH solution, including metal (Cs^+ , Tb^{3+} , Dy^{3+} , Ho^{3+} , Er^{3+} , Tm^{3+}) salts. After standing for 12 hours, five-element $\text{Cs}_3\{\text{TbDyHoErTm}\}_1\text{Cl}_6$ metal halide crystals were successfully acquired at room temperature (Fig. 2c). High-resolution transmission electron microscopy (HRTEM) exhibits distinct lattice fringes with a lattice spacing of 0.29 nm that is indexed as crystal plane

($\bar{6}22$) of the $\text{Cs}_3\{\text{TbDyHoErTm}\}_1\text{Cl}_6$ crystals phase (Fig. 2d). SEM elemental mappings reveal homogeneous distribution of all five incorporated Ln^{3+} ions within five-element $\text{Cs}_3\{\text{TbDyHoErTm}\}_1\text{Cl}_6$ crystals (Fig. 2e). In Supplementary Table S2, inductively coupled plasma optical emission spectrometry (ICP-OES) provided the actual molar ratio of the five Ln^{3+} ions (at 17–25%). The XRD pattern of as-prepared five-element $\text{Cs}_3\{\text{TbDyHoErTm}\}_1\text{Cl}_6$ crystals displays a similar monoclinic structure with the physical mixture of five corresponding single-element crystals (Fig. 2f). Moreover, after fine scanning the primary characteristic diffraction peak, no peak splitting happens and the full width at half maximum (FWHM) displays a smaller value compared with that of the physical mixture with the multi-phase structure, implying the single-phase structure of $\text{Cs}_3\{\text{TbDyHoErTm}\}_1\text{Cl}_6$ crystals. As a result, as-prepared $\text{Cs}_3\{\text{TbDyHoErTm}\}_1\text{Cl}_6$ crystals could be confirmed as single-phase

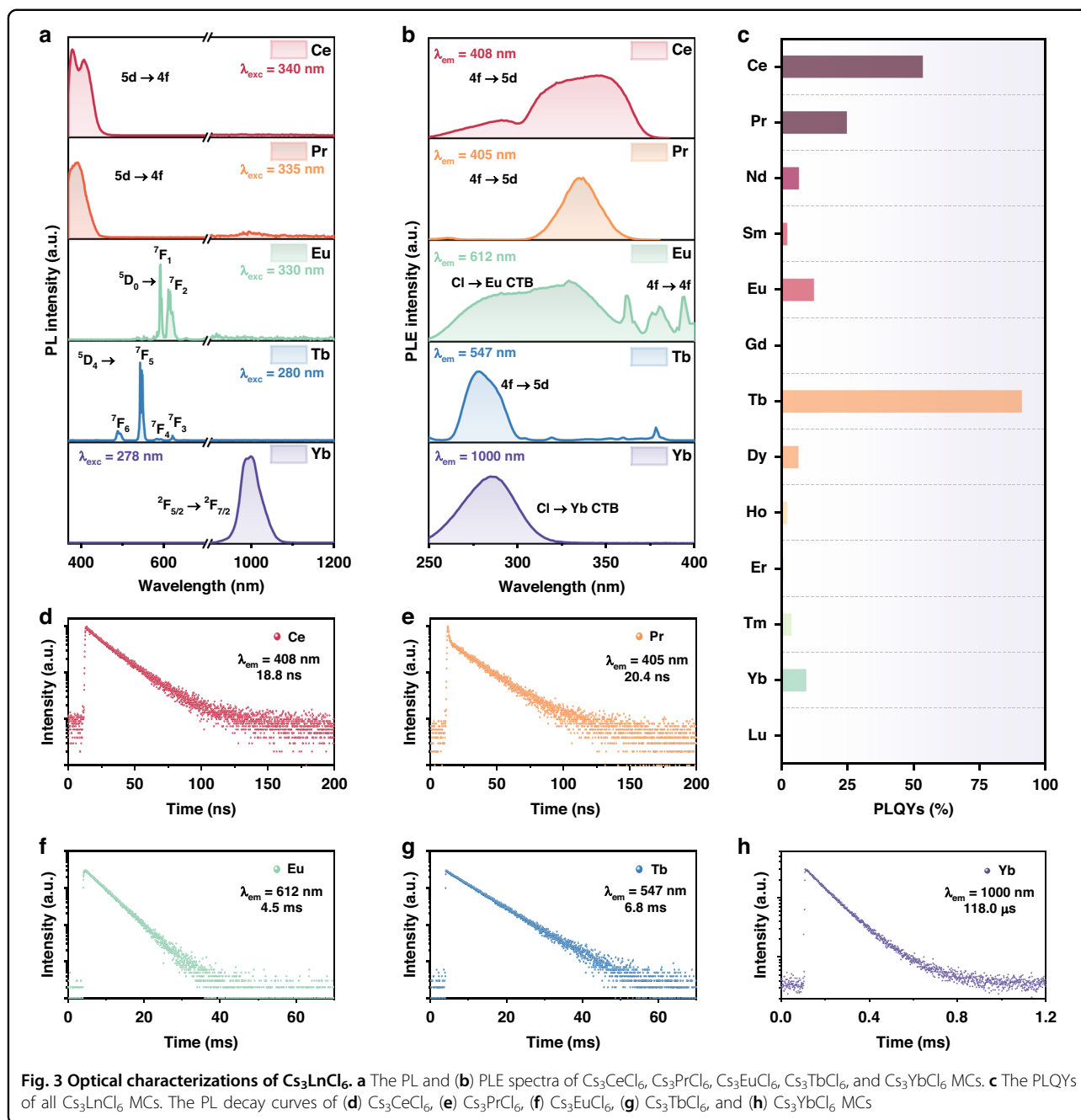


high-entropy crystals, indicating that high-entropy Ln-based metal halide crystals could be successfully prepared at room temperature based on this recrystallization method.

To investigate the optical properties of as-prepared Cs_3LnCl_6 MCs, the absorption spectra are carried out (Supplementary Fig. S17). The absorption bands located at 340 nm for Cs_3CeCl_6 and 285 nm for Cs_3TbCl_6 could be ascribed to $4f \rightarrow 5d$ transitions of Ce^{3+} and Tb^{3+} ions, respectively. In the absorption spectrum of Cs_3PrCl_6 , there are a weak broadband (300–420 nm) and sharp peaks (420–600 nm), which could be attributed to $4f \rightarrow 5d$ and $4f \rightarrow 4f$ transitions of Pr^{3+} ions, respectively. For Cs_3EuCl_6 and Cs_3YbCl_6 , the broad absorption bands are charge transfer bands (CTB) in $[\text{EuCl}_6]^{3-}$ and $[\text{YbCl}_6]^{3-}$ octahedra. While for other Cs_3LnCl_6 , there are mainly sharp peaks from $4f \rightarrow 4f$ transitions of Ln^{3+} ions or no obvious absorption peaks. The parity forbidden $4f \rightarrow 4f$ transitions of Cs_3LnCl_6 MCs may limit their photoluminescence (PL) performance and optoelectronic applications. Then, PL spectra of these Cs_3LnCl_6 MCs under the excitations of specific wavelengths are shown in Fig. 3a, Supplementary Figs. S18 and S19. Among these MCs, Cs_3CeCl_6 , Cs_3PrCl_6 , Cs_3TbCl_6 , and Cs_3EuCl_6 possess the strongest visible emissions and emit bright blue (around 400 nm; Cs_3CeCl_6 and Cs_3PrCl_6), green (547 nm; Cs_3TbCl_6), and red (592 nm and 612 nm; Cs_3EuCl_6) emissions, respectively. In the NIR range, Cs_3YbCl_6 MCs display the strongest emission at

~1000 nm. While for other Cs_3LnCl_6 , only weak Ln^{3+} characteristic emissions or host emissions could be observed. The PLE spectra of Cs_3LnCl_6 MCs monitored at the position of Ln^{3+} characteristic emissions are shown in Fig. 3b and Supplementary Fig. S20, the excitation bands display similar patterns with their absorption spectra. Then, under the excitation of specific wavelength, absolute PLQYs of these Cs_3LnCl_6 MCs could be obtained (Fig. 3c and Supplementary Table S3). Among them, Cs_3TbCl_6 possesses the highest PLQY of 90.8%, exceeding most lead-free metal halides (Supplementary Table S4)^{33–39}. From the values of PLQYs, among all Cs_3LnCl_6 MCs, those Cs_3LnCl_6 ($\text{Ln} = \text{Ce}, \text{Pr}, \text{Eu}, \text{Tb}, \text{Yb}$) with great absorption ability usually possess great PL performance as well. In Fig. 3d–h and Supplementary Fig. S21, the PL decay curves of Ln^{3+} characteristic emissions or host emissions in Cs_3LnCl_6 could provide their lifetimes that match the characteristics of the lifetimes of $5d/4f \rightarrow 4f$ transitions of Ln^{3+} ions.

To further investigate the great absorption abilities in parts of Cs_3LnCl_6 . The electronic structures of Cs_3LnCl_6 were investigated by theory calculation. The partial charge density maps and partial density of states (PDOS) of Cs_3CeCl_6 and Cs_3EuCl_6 were carried out for Ce^{3+} and Eu^{3+} act as typical Ln^{3+} ions to display $4f \rightarrow 5d$ transition and $\text{Cl} \rightarrow \text{Ln}$ charge transfer transition, respectively (Fig. 4a–d). As disclosed in the partial charge density maps and PDOS of Cs_3CeCl_6 , the valence band (VB) was composed of Cl-3p and Ce-4f



occupied orbitals. While the conduction band (CB) was composed of Ce-5d and Ce-4f empty orbitals. For comparison, the PDOS of Cs_3LnCl_6 (Ln = Pr, Nd, Sm, and Gd) are also calculated (Supplementary Fig. S22). It is found that the 4f occupied orbitals are much closer to 5d empty orbitals in Cs_3CeCl_6 , which could be responsible for their greater possibility for 4f \rightarrow 5d transitions. For Cs_3EuCl_6 , the VB and CB are contributed by Cl-3p occupied orbitals and Eu-4f empty orbitals, respectively. Similarly, the Eu-4f empty orbitals are much closer to Cl-3p occupied orbitals in Cs_3EuCl_6 , implying a higher possibility for Cl \rightarrow Eu charge transfer transitions.

Tb^{3+} and Pr^{3+} ions could display 4f \rightarrow 5d transitions, and Yb^{3+} ions possess Cl \rightarrow Yb charge transfer transition as well, which may be attributed to the similar energy level conditions with that of Cs_3CeCl_6 and Cs_3EuCl_6 , respectively. In Fig. 4e, the possible PL mechanisms of these Cs_3LnCl_6 (Ln = Ce, Pr, Tb, Eu, and Yb) with 4f \rightarrow 5d transitions or charge transfer transitions are proposed. For Cs_3CeCl_6 and Cs_3PrCl_6 , the electrons in the 4f ground states are excited to the 5d excited states and then relaxed to the 4f ground states, giving out blue emissions due to 5d \rightarrow 4f radiative recombination. For Cs_3TbCl_6 , after being excited from 4f

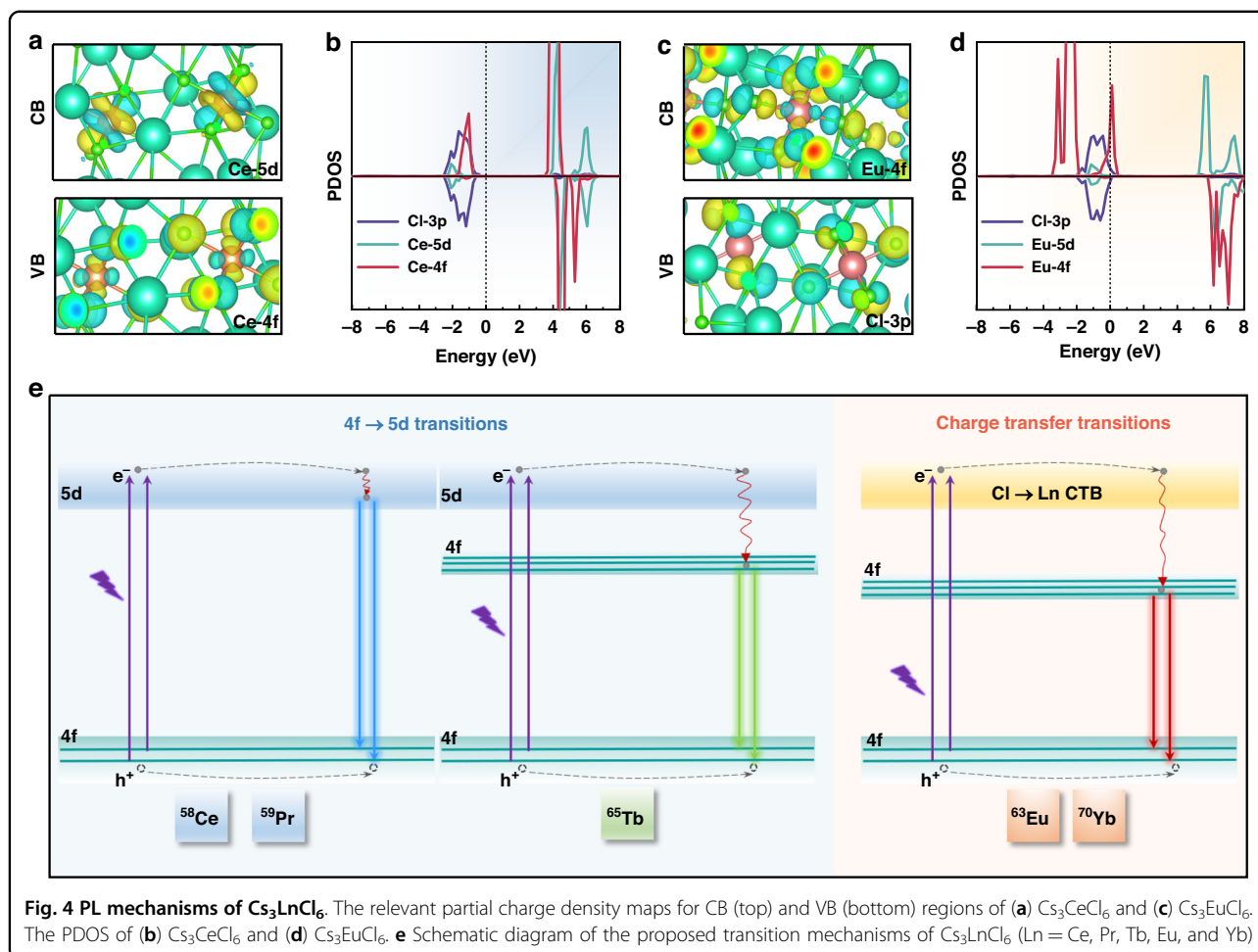


Fig. 4 PL mechanisms of Cs_3LnCl_6 . The relevant partial charge density maps for CB (top) and VB (bottom) regions of (a) Cs_3CeCl_6 and (c) Cs_3EuCl_6 . The PDOS of (b) Cs_3CeCl_6 and (d) Cs_3EuCl_6 . **e** Schematic diagram of the proposed transition mechanisms of Cs_3LnCl_6 (Ln = Ce, Pr, Tb, Eu, and Yb)

ground state to the 5d excited state, the electrons are non-radiatively relaxed to the Tb^{3+} 4f excited states and further relaxed to 4f ground states along with Tb^{3+} characteristic emissions from 4f \rightarrow 4f transitions. While for Cs_3EuCl_6 and Cs_3YbCl_6 , after being excited from Ln^{3+} 4f ground states to charge transfer states, the electrons are relaxed to Ln^{3+} 4f excited states and then relaxed to 4f ground states, resulting in corresponding Ln^{3+} emissions for radiative recombination of their 4f \rightarrow 4f transitions.

For other Cs_3LnCl_6 without 4f \rightarrow 5d transitions or charge transfer transitions, their 4f occupied orbitals may be far away from 5d empty orbitals, and their 4f empty orbitals may be far from Cl-3p occupied orbitals, resulting in higher energy required for 4f \rightarrow 5d transitions and Cl \rightarrow Ln charge transfer transitions, thus decreasing the probability for these transitions under the excitation of near UV light. Therefore, it is difficult for these Cs_3LnCl_6 to exhibit great absorption ability based on 4f \rightarrow 5d transitions or Cl \rightarrow Ln charge transfer transitions. Hence, among all Cs_3LnCl_6 , small energy level intervals from Ln-4f occupied orbitals to Ln-5d empty orbitals or from Cl-3p occupied orbitals to Ln-4f empty orbitals could result

in great possibilities for 4f \rightarrow 5d transitions or Cl \rightarrow Ln charge transfer transitions that replace the parity forbidden 4f \rightarrow 4f transitions and could be responsible for their great PL performance.

The thermogravimetric (TG) curves (Supplementary Fig. S23) show no significant weight loss (remaining > 94%) until 600 $^{\circ}\text{C}$ for these Cs_3LnCl_6 MCs, indicating their excellent structural stability. In Supplementary Figs. S24 and S25, the PL intensities of Cs_3LnCl_6 MCs remain above 88% of their initial values, and XRD patterns remain essentially unchanged after the MCs were left in a sealed environment without light exposure for 300 days, indicating the great air stability of these Cs_3LnCl_6 MCs.

The light yield (LY), as one of the important indicators for evaluating the scintillator performance, is proportional to the PLQYs of scintillators. Among these Cs_3LnCl_6 , Cs_3TbCl_6 MCs with the highest PLQY and large Stokes shift could be very promising to exhibit great scintillator performance and have great potential for X-ray imaging⁴⁰. Therefore, the X-ray scintillation performance of Cs_3TbCl_6 MCs was explored. The band gap of Cs_3TbCl_6 was calculated as 4.3 eV in Supplementary Fig. S26.

Compared with commercially available scintillators, Cs_3TbCl_6 MCs exhibit a higher absorption coefficient than that of NaI:Tl and the equivalent absorption coefficient with that of $\text{Lu}_3\text{Al}_5\text{O}_{12}:\text{Ce}$ (LuAG:Ce) at 8–10 keV (Fig. 5a). For quantifying the X-ray LY of Cs_3TbCl_6 MCs, commercially available scintillator LuAG:Ce (with the thickness of 1 mm; the LY of 25,000 photons MeV^{-1}) was selected as the reference^{40,41}. Meantime, as shown in Supplementary Fig. S27a, Cs_3TbCl_6 sample with the thickness of 0.5 mm was prepared to unify the absorbed X-ray energy with LuAG:Ce sample. Radioluminescence (RL) spectra of Cs_3TbCl_6 MCs and LuAG:Ce are presented in Fig. 5b, similar Tb^{3+} characteristic emissions of Cs_3TbCl_6 imply the same radiative recombination channel with that under the excitation of UV light. Besides, as the X-ray dose rate increases, the RL integral intensity of Cs_3TbCl_6 MCs displays a linear increasing response curve (Supplementary Fig. S27b). As exhibited in Fig. 5c, the response of Cs_3TbCl_6 MCs is 2.07 times higher than that of LuAG:Ce and the outstanding LY of Cs_3TbCl_6 MCs is $\sim 51,800$ photons MeV^{-1} . Compared with other Ln-based metal halide scintillators obtained via solid-state synthesis, hydrothermal synthesis or hot-injection methods in previous reports, as-prepared Cs_3TbCl_6 MCs could not only be synthesized quickly under mild synthetic conditions but also possess excellent LY of X-ray scintillator (Fig. 5d and Supplementary Table S5)^{22,28,33,42}. Meantime, as shown in Supplementary Fig. S27c, the LY of Cs_3TbCl_6 MCs exceeds that of parts of commercial scintillation crystals^{43–45}. Moreover, compared with commercial scintillation crystals $\text{Gd}_2\text{O}_2\text{S:Ce,Pr,F}$ (LY = 35000 photons MeV^{-1}), Cs_3TbCl_6 MCs with higher LY have great potential to replace $\text{Gd}_2\text{O}_2\text{S:Ce,Pr,F}$ and be used as the next generation sensitization screen in the field of X-ray computed tomography imaging. In Supplementary Fig. S27d, when the signal-to-noise ratio (SNR) is 3, the detection limit of Cs_3TbCl_6 MCs is 63 nGy s^{-1} , which is 87.3 times lower than those required for medical X-ray diagnosis standards ($5.5 \mu\text{Gy s}^{-1}$)⁴⁶. Furthermore, under the X-ray irradiation with a cumulative dose of 1.38 Gy, the RL intensity remains unchanged, demonstrating the robust radiation hardness of Cs_3TbCl_6 MCs as X-ray scintillators (Fig. 5e). Subsequently, for X-ray imaging, flexible scintillation thin film ($50 \text{ mm} \times 50 \text{ mm} \times 1 \text{ mm}$) based on Cs_3TbCl_6 MCs powder was prepared via blending the sample with polydimethylsiloxane (PDMS) and put it in X-ray imaging system (Fig. 5f and Supplementary Fig. S27e). As shown in Fig. 5g–i, a smartphone, a headset, and a wireless network interface controller were utilized as target objects to research the X-ray imaging ability of $\text{Cs}_3\text{TbCl}_6@\text{PDMS}$ film. Under X-ray illumination, the distinct inside structure can be distinguished, indicating the realization of non-destructive

testing for internal electronic components in these target objects. As presented in line-pair card imaging in Fig. 5j, the spatial resolution is derived as 12 lp mm^{-1} , exceeding that of most scintillator thin films based on Ln-based metal halides in the previous reports (Supplementary Table S6)^{22,27,28,42}. It is suggested that Cs_3TbCl_6 MCs synthesized by the recrystallization method possess excellent scintillator performance and have great potential for X-ray imaging.

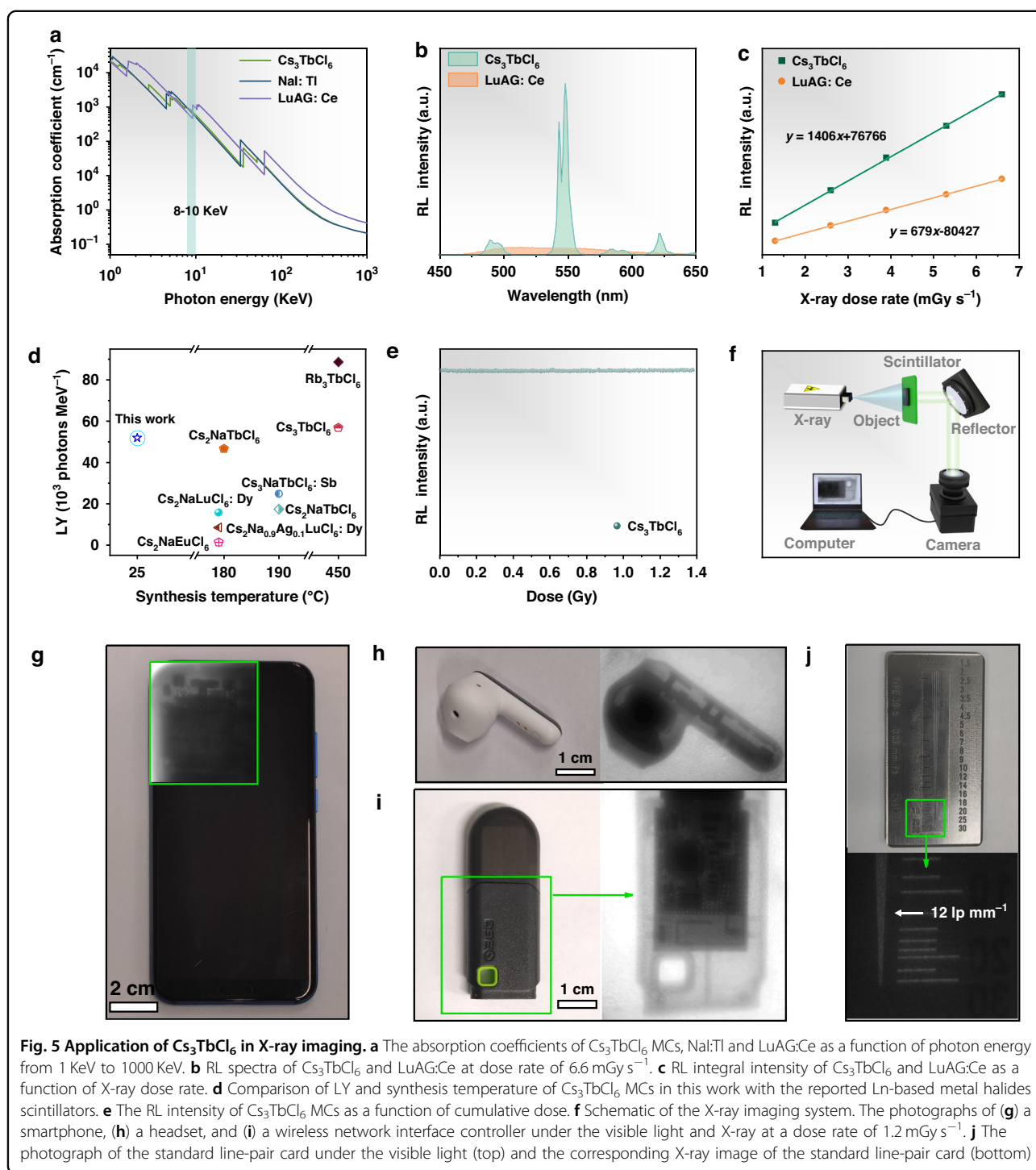
Discussion

In summary, we have prepared a series of Cs_3LnCl_6 MCs through a facile recrystallization method at room temperature for the first time. Especially, based on this method, large-scale production at one time and multiple recyclable recrystallizations of single-element Cs_3LnCl_6 MCs and the preparation of high-entropy five-element $\text{Cs}_3\{\text{TbDy-HoErTm}\}_1\text{Cl}_6$ metal halide crystals could also be realized. Based on DFT calculations, low energy for $4f \rightarrow 5d$ transitions or $\text{Cl} \rightarrow \text{Ln}$ charge transfer transitions could overcome the $4f \rightarrow 4f$ parity forbidden transitions of Ln^{3+} and bring excellent absorption ability and great PL performance of Cs_3LnCl_6 MCs. Especially, Cs_3TbCl_6 with $4f \rightarrow 5d$ transitions absorption band possesses the highest PLQY of 90.8% among these Cs_3LnCl_6 MCs. Under X-ray irradiation, Cs_3TbCl_6 MCs show excellent X-ray scintillation performance with a high LY of $\sim 51,800$ photons MeV^{-1} and the as-fabricated $\text{Cs}_3\text{TbCl}_6@\text{PDMS}$ thin films possess promising X-ray imaging ability and preferable spatial resolution (12 lp mm^{-1}). This work displays a novel recrystallization method for ultrafast and mild preparation of Ln-based metal halides and highlights their excellent potential as scintillators for X-ray imaging.

Materials and methods

Chemicals

Cesium chloride (CsCl , 99.99%), Cerium chloride heptahydrate ($\text{CeCl}_3 \cdot 7\text{H}_2\text{O}$, 99%), praseodymium chloride hydrate ($\text{PrCl}_3 \cdot x\text{H}_2\text{O}$, 99.9%), neodymium chloride (NdCl_3 , 99.9%), samarium chloride hydrate ($\text{SmCl}_3 \cdot x\text{H}_2\text{O}$, 99.99%), Europium chloride hydrate ($\text{EuCl}_3 \cdot x\text{H}_2\text{O}$, 99.9%), gadolinium chloride hexahydrate ($\text{GdCl}_3 \cdot 6\text{H}_2\text{O}$, 99.9%), terbium chloride hexahydrate ($\text{TbCl}_3 \cdot 6\text{H}_2\text{O}$, 99.99%), dysprosium chloride hydrate ($\text{DyCl}_3 \cdot x\text{H}_2\text{O}$, 99.99%), holmium chloride hexahydrate ($\text{HoCl}_3 \cdot 6\text{H}_2\text{O}$, 99.9%), erbium chloride hydrate ($\text{ErCl}_3 \cdot x\text{H}_2\text{O}$, 99.99%), thulium chloride hydrate ($\text{TmCl}_3 \cdot x\text{H}_2\text{O}$, 99.9%), ytterbium chloride hydrate ($\text{YbCl}_3 \cdot x\text{H}_2\text{O}$, 99.9%), lutetium chloride hexahydrate ($\text{LuCl}_3 \cdot 6\text{H}_2\text{O}$, 99.9%) were purchased from Alfa Aesar. Methanol (MeOH , AR) and ethanol (EtOH , AR) were purchased from XiLONG SCIENCE. Polydimethylsiloxane (PDMS, SYLGARD® 184) was purchased from Dow Corning. All the chemicals were commercially purchased and used without further purification.



Preparation of Cs_3LnCl_6 MCs

0.6 mmol CsCl was first dissolved in 4 mL of methanol under ultrasound. 0.2 mmol $\text{LnCl}_3 \cdot x\text{H}_2\text{O}$ was dissolved in 1 mL of methanol. Then, the above two solutions were mixed evenly. After introducing 5 mL of ethanol into the mixture, white precipitate formed immediately. After standing for 2 min, the supernatant was discarded, the

collected precipitation was dried at 60°C for 10 min to obtain Cs_3LnCl_6 MCs.

Preparation of $\text{Cs}_3\{\text{TbDyHoErTm}\}_1\text{Cl}_6$ high entropy crystals

0.6 mmol CsCl was first dissolved in 4 mL of methanol under ultrasound. 0.04 mmol $\text{TbCl}_3 \cdot 6\text{H}_2\text{O}$, 0.04 mmol $\text{DyCl}_3 \cdot x\text{H}_2\text{O}$, 0.04 mmol $\text{HoCl}_3 \cdot 6\text{H}_2\text{O}$, 0.04 mmol

$\text{ErCl}_3 \cdot x\text{H}_2\text{O}$ and 0.04 mmol $\text{TmCl}_3 \cdot x\text{H}_2\text{O}$ were dissolved in 1 mL of methanol. Then, the above two solutions were mixed evenly. Subsequently, an appropriate amount of ethanol was slowly diffused into the methanol solution for 12 h to form the transparent white crystals. Then, the supernatant was discarded, and the collected precipitation was dried at 60 °C for 10 min to obtain $\text{Cs}_3\{\text{TbDy-HoErTm}\}_1\text{Cl}_6$ high entropy crystals.

Preparation of Cs_3TbCl_6 @PDMS flexible thin film

First, 2.270 g of PDMS base resin and 0.2300 g of curing agent were mixed in a beaker. Then, 0.1880 g of Cs_3TbCl_6 powder was dispersed in the above PDMS precursor with stirring for 30 min. After curing at 100 °C for 60 min, the Cs_3TbCl_6 @PDMS flexible thin film was obtained.

Acknowledgements

This work was supported by financial aid from the National Natural Science Foundation of China (22271273).

Author details

¹State Key Laboratory of Rare Earth Resource Utilization, Changchun Institute of Applied Chemistry, Chinese Academy of Sciences, Changchun 130022, China. ²State Key Laboratory of Inorganic Synthesis and Preparative Chemistry, College of Chemistry, Jilin University, Changchun 130012, China. ³School of Applied Chemistry and Engineering, University of Science and Technology of China, Hefei 230026, China. ⁴Department of Chemistry, Tsinghua University, Beijing 100084, China

Author contributions

H. L., J. F., S. S. and H. Z. designed the experiments, interpreted the data, and co-wrote the paper. H. L. carried out the syntheses, characterization studies, and data analyses. K. L. interpreted the theoretical results. Z. L., X. F., Q. Y. and N. W. participated in the measurement and data analyses. K. L. and X. W. gave suggestions on writing the paper. J. F., S. S. and H. Z. discussed the results and commented on the paper.

Data availability

Data will be available when the paper is officially published.

Conflict of interest

The authors declare no competing interests.

Supplementary information The online version contains supplementary material available at <https://doi.org/10.1038/s41377-025-01839-5>.

Received: 23 September 2024 Revised: 19 March 2025 Accepted: 20 March 2025

Published online: 14 May 2025

References

- Chen, Q. S. et al. All-inorganic perovskite nanocrystal scintillators. *Nature* **561**, 88–93 (2018).
- Mi, Z. H. et al. Real-time single-proton counting with transmissive perovskite nanocrystal scintillators. *Nat. Mater.* **23**, 803–809 (2024).
- Yi, L. Y. et al. A double-tapered fibre array for pixel-dense gamma-ray imaging. *Nat. Photonics* **17**, 494–500 (2023).
- Cho, S. et al. Hybridisation of perovskite nanocrystals with organic molecules for highly efficient liquid scintillators. *Light* **9**, 156 (2020).
- Pang, J. C. et al. Vertical matrix perovskite X-ray detector for effective multi-energy discrimination. *Light* **11**, 105 (2022).
- Jin, T. et al. Self-wavelength shifting in two-dimensional perovskite for sensitive and fast gamma-ray detection. *Nat. Commun.* **14**, 2808 (2023).
- Lian, H. W. et al. Aqueous-based inorganic colloidal halide perovskites customizing liquid scintillators. *Adv. Mater.* **35**, 2304743 (2023).
- Marshall, K. P. et al. Enhanced stability and efficiency in hole-transport-layer-free CsSnI_3 perovskite photovoltaics. *Nat. Energy* **1**, 16178 (2016).
- Park, Y. et al. Designing zero-dimensional dimer-type all-inorganic perovskites for ultra-fast switching memory. *Nat. Commun.* **12**, 3527 (2021).
- Luo, J. J. et al. Efficient and stable emission of warm-white light from lead-free halide double perovskites. *Nature* **563**, 541–545 (2018).
- Saikia, S., Ghosh, A. & Nag, A. Broad dual emission by codoping $\text{Cr}^{3+}(\text{d} \rightarrow \text{d})$ and $\text{Bi}^{3+}(\text{s} \rightarrow \text{p})$ in $\text{Cs}_2\text{Ag}_{0.6}\text{Na}_{0.4}\text{InCl}_6$ double perovskite. *Angew. Chem. Int. Ed.* **62**, e202307689 (2023).
- Yang, H. X. et al. A universal hydrochloric acid-assistant powder-to-powder strategy for quick and mass preparation of lead-free perovskite microcrystals. *Light* **12**, 75 (2023).
- Li, H. W. et al. Efficient multi-luminescence covering the visible to near-infrared range in antimony and lanthanide co-doped indium-based zero-dimensional perovskites nanocrystals. *Adv. Opt. Mater.* **11**, 2300429 (2023).
- Chen, J. K. et al. Ultrafast and multicolor luminescence switching in a lanthanide-based hydrochromic perovskite. *J. Am. Chem. Soc.* **144**, 22295–22301 (2022).
- Jin, S. L. et al. Compact ultrabroadband light-emitting diodes based on lanthanide-doped lead-free double perovskites. *Light* **11**, 52 (2022).
- Li, H. W. et al. Double perovskite $\text{Cs}_2\text{NaNCl}_6$ nanocrystals with intense dual-emission via self-trapped exciton-to- Tb^{3+} dopant energy transfer. *J. Mater. Chem. C* **10**, 10609–10615 (2022).
- Li, H. W. et al. Multiple energy transfer channels in rare earth doped multi-exciton emissive perovskites. *Adv. Sci.* **11**, 2307354 (2024).
- Wang, X. J. et al. Nearly-unity quantum yield and 12-hour afterglow from a transparent perovskite of $\text{Cs}_2\text{NaScCl}_6\text{:Tb}$. *Angew. Chem. Int. Ed.* **61**, e202210853 (2022).
- Dang, P. P. et al. Red-NIR luminescence in rare-earth and manganese ions Codoped $\text{Cs}_2\text{CdBi}_2\text{Cl}_{12}$ vacancy-ordered quadruple perovskites. *Chem. Mater.* **35**, 1640–1650 (2023).
- Wang, H. Y. et al. Simultaneously achieving multicolor emission of downshifting and up-conversion in Yb^{3+} , Er^{3+} -Codoped $\text{Cs}_2\text{NaGdCl}_6$ double perovskites. *Adv. Opt. Mater.* **11**, 2300694 (2023).
- Shi, Y. H. et al. Pure green upconversion from a multicolor downshifting perovskite crystal. *Adv. Opt. Mater.* **11**, 2202704 (2023).
- Zhang, N. et al. X-ray-activated long afterglow double-perovskite scintillator for detection and extension imaging. *Adv. Opt. Mater.* **11**, 2300187 (2023).
- Li, H. et al. A solar-blind perovskite scintillator realizing portable X-ray imaging. *ACS Energy Lett.* **7**, 2876–2883 (2022).
- Kachhap, S. et al. Expanding the emission of CsPbBr_3 nanocrystals in the blue region. *ACS Appl. Opt. Mater.* **1**, 1974–1986 (2023).
- Zeng, Z. C. et al. Rare-earth-based perovskite $\text{Cs}_2\text{AgScCl}_6\text{:Bi}$ for strong full visible spectrum emission. *Adv. Funct. Mater.* **32**, 2204780 (2022).
- Sun, L. H. et al. Efficient and stable multicolor emissions of the coumarin-modified Cs_2LnCl_6 lead-free perovskite nanocrystals and LED application. *Adv. Mater.* **36**, 2310065 (2024).
- Zhou, W. et al. Sb-doped Cs_3TbCl_6 nanocrystals for highly efficient narrow-band green emission and X-ray imaging. *Adv. Mater.* **36**, 2302140 (2024).
- Han, J. H. et al. Highly stable zero-dimensional lead-free metal halides for X-ray imaging. *ACS Energy Lett.* **8**, 545–552 (2023).
- Han, J. H. et al. Intense hydrochromic photon upconversion from lead-free 0D metal halides for water detection and information encryption. *Adv. Mater.* **35**, 2302442 (2023).
- Reddy, M. M. & Hoch, A. R. Calcite crystal growth rate inhibition by polycarboxylic acids. *J. Colloid Interface Sci.* **235**, 365–370 (2001).
- Luo, Y. B. et al. High thermoelectric performance in the new cubic semiconductor AgSnSbSe_3 by high-entropy engineering. *J. Am. Chem. Soc.* **142**, 15187–15198 (2020).
- Deng, Z. H. et al. Semiconducting high-entropy chalcogenide alloys with ambivalent entropy stabilization and ambipolar doping. *Chem. Mater.* **32**, 6070–6077 (2020).
- Hu, Q. S. et al. X-ray scintillation in lead-free double perovskite crystals. *Sci. China Chem.* **61**, 1581–1586 (2018).
- Wang, L. et al. Exploration of nontoxic Cs_2CeBr_6 for violet light-emitting diodes. *ACS Energy Lett.* **6**, 4245–4254 (2021).

35. Luo, J. J. et al. Efficient blue light emitting diodes based on europium halide perovskites. *Adv. Mater.* **33**, 2101903 (2021).
36. Chen, B. et al. Multiexcitonic emission in zero-dimensional $\text{Cs}_2\text{ZrCl}_6\text{Sb}^{3+}$ perovskite crystals. *J. Am. Chem. Soc.* **143**, 17599–17606 (2021).
37. Wu, R. Y. et al. Red-emitting perovskite variant Cs_2PtCl_6 phosphor: material design, luminous mechanism, and application in high-color-rendering white light-emitting diodes. *Adv. Opt. Mater.* **10**, 2201081 (2022).
38. Kong, Q. K. et al. Phase engineering of cesium manganese bromides nanocrystals with color-tunable emission. *Angew. Chem. Int. Ed.* **60**, 19653–19659 (2021).
39. Wei, J. H. et al. All-inorganic lead-free heterometallic $\text{Cs}_4\text{MnBi}_2\text{Cl}_{12}$ perovskite single crystal with highly efficient orange emission. *Matter* **3**, 892–903 (2020).
40. Han, K. et al. Promoting single channel photon emission in Copper(I) halide clusters for X-ray detection. *Adv. Opt. Mater.* **10**, 2200865 (2022).
41. Han, K. et al. Seed-crystal-induced cold sintering toward metal halide transparent ceramic scintillators. *Adv. Mater.* **34**, 2110420 (2022).
42. Zhou, W. et al. Bright green-emitting all-inorganic terbium halide double perovskite nanocrystals for low-dose X-ray imaging. *J. Phys. Chem. Lett.* **14**, 8577–8583 (2023).
43. Michail, C. et al. Measurement of the luminescence properties of $\text{Gd}_2\text{O}_2\text{S:Pr,Ce,F}$ powder scintillators under X-ray radiation. *Radiat. Meas.* **70**, 59–64 (2014).
44. He, T. Y. et al. High-performance copper-doped perovskite-related silver halide X-ray imaging scintillator. *ACS Energy Lett.* **7**, 2753–2760 (2022).
45. Jin, J. C. et al. Zn^{2+} doping in organic manganese(II) bromide hybrid scintillators toward enhanced light yield for X-ray imaging. *Adv. Opt. Mater.* **11**, 2300330 (2023).
46. Wei, H. T. et al. Sensitive X-ray detectors made of methylammonium lead tribromide perovskite single crystals. *Nat. Photonics* **10**, 333–339 (2016).